

Ultrahighly Alkali-Tolerant NO_x Reduction over Self-Adaptive $\text{CePO}_4/\text{FePO}_4$ Catalysts

Zhi Shen, Penglu Wang, Xiaonan Hu, Wenqiang Qu, Xiangyu Liu, and Dengsong Zhang*



Cite This: *Environ. Sci. Technol.* 2023, 57, 14472–14481



Read Online

ACCESS |

Metrics & More

Article Recommendations

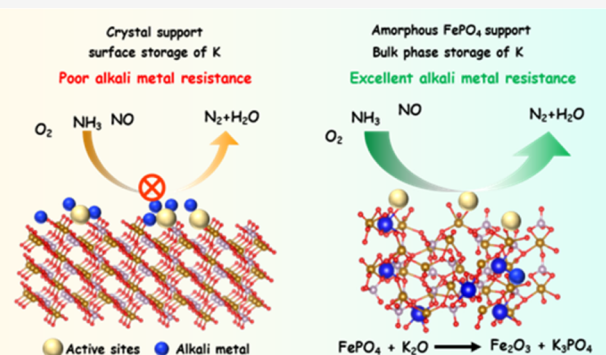
Supporting Information

ABSTRACT: Catalyst deactivation caused by alkali metal poisoning has long been a key bottleneck in the application of selective catalytic reduction of NO_x with NH_3 ($\text{NH}_3\text{-SCR}$), limiting the service life of the catalyst and increasing the cost of environmental protection. Despite great efforts, continuous accumulation of alkali metal deposition makes the resistance capacity of 2 wt % K_2O difficult to enhance via merely loading acid sites on the surface, resulting in rapid deactivation and frequent replacement of the $\text{NH}_3\text{-SCR}$ catalyst. To further improve the resistance of alkali metals, encapsulating alkali metals into the bulk phase could be a promising strategy. The bottleneck of 2 wt % K_2O tolerance has been solved by virtue of ultrahigh potassium storage capacity in the amorphous FePO_4 bulk phase. Amorphous FePO_4 as a support of the $\text{NH}_3\text{-SCR}$ catalyst exhibited a self-adaptive alkali-tolerance mechanism, where potassium ions spontaneously migrated into the bulk phase of amorphous FePO_4 and were anchored by PO_4^{3-} with the generation of Fe_2O_3 at the $\text{NH}_3\text{-SCR}$ reaction temperature. This ingenious potassium storage mechanism could boost the K_2O resistance capacity to 6 wt % while maintaining approximately 81% NO_x conversion. Besides, amorphous FePO_4 also exhibited excellent resistance to individual and coexistence of alkali (K_2O and Na_2O), alkali earth (CaO), and heavy metals (PbO and CdO), providing long durability for $\text{CePO}_4/\text{FePO}_4$ catalysts in flue gas with multipollutants. The cheap and accessible amorphous FePO_4 paves the way for the development and implementation of poisoning-resistant NO_x abatement.

KEYWORDS: air pollution control, NO_x reduction, alkali metal resistance, selective catalytic reduction, environmental catalysis

INTRODUCTION

Increasing nitrogen oxide (NO_x) emissions have significantly harmed the ecological environment and human health.^{1–3} Selective catalytic reduction of NO_x with NH_3 ($\text{NH}_3\text{-SCR}$) is an effective technology for responding to strict environmental protection policies.^{4–7} However, among stationary NO_x emission sources such as waste incineration, coal-fired power, and other industrial furnaces, a mass of alkali metals existing in flue gas dust, including corresponding oxides, chlorines, and sulfates, greatly shorten the service life of catalysts and increase the expenditure of environmental protection.^{8–10} The poisoning mechanisms of alkali metals are attributed to strong competitive adsorption with NH_3 on acid sites and severe inhibition of oxidation capacity via the electron donation effect, resulting in failing to adsorb reactants and complete the redox cycle on catalysts.¹¹ In order to cope with the poisoning of alkali metals, the principle of acid–base neutralization is frequently employed in the design and manufacturing of catalysts for $\text{NH}_3\text{-SCR}$.⁹ The common technical paths during catalyst preparation were (I) adding acid additives, such as metal oxides (WO_3 , MoO_3 , Nb_2O_5 , etc.), heteropoly acids ($\text{H}_3\text{PW}_{12}\text{O}_{40}$, $\text{H}_3\text{PMo}_{12}\text{O}_{40}$, etc.),^{12,13} and inorganic acids



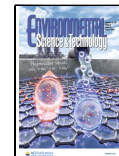
(H_2SO_4 , $(\text{NH}_4)_2\text{SO}_4$, H_3PO_4 , etc.) to neutralize alkali metals^{14–18} and (II) designing porous structures with internal H^+ (hollandite manganese oxides, hexagonal WO_3 , etc.) to anchor alkali metals via ion exchange benefited from the virtue of low Tammann temperature for potassium.^{19–22} For strategy I, the introduction of the acid additives only works on the surface of the catalyst, leading to the constrained acid amounts and the unsatisfactory alkali resistance capacity (ca. 1 wt %), which limits the SCR performance maintaining under higher content of alkali metal accumulation.^{9,19,23–27} For strategy II, the construction of the porous structure achieves acceptable alkali resistance capacity up to ca. 4.5 wt % due to alkali metal storage in the bulk phase.¹⁹ However, strategy II might have the disadvantages of high manufacturing cost and poor N_2 selectivity. Therefore, developing an economic strategy that

Received: June 30, 2023

Revised: August 13, 2023

Accepted: August 28, 2023

Published: September 11, 2023



can tremendously promote the resistance of alkali metals is substantial and urgent for NO_x reduction under complex flue gases.

Fortunately, amorphous FePO_4 in batteries could achieve an ultrahigh potassium storage capacity of $143 \text{ mA}\cdot\text{h}\cdot\text{g}^{-1}$ (equal to ca. 20.8 wt %).^{28–30} Inspired by the potassium-ion battery materials, accessible amorphous FePO_4 might be a promising candidate via bulk storage to enhance potassium storage capacity in NH_3 -SCR. In a battery, the electric field could impel potassium into the bulk phase of FePO_4 . Will similar mechanisms of bulk-phase potassium storage in nonelectric NH_3 -SCR still exist when adopting amorphous FePO_4 ? Besides, only FePO_4 was of low active nature and needed to be coupled with other active components to improve NH_3 -SCR activity while maintaining ultrahigh potassium tolerance. If the active components are metal oxides, the active metal oxides would bond with leaching PO_4^{3-} due to the high solubility product (K_{sp}) of FePO_4 to produce inactive phosphates (such as $\text{Mn}_3(\text{PO}_4)_2$, $\text{Cu}_3(\text{PO}_4)_2$) in the wet preparation procedure with water. In order to illustrate the genuine antipotassium mechanism, the active components might be selected as active phosphates (such as CePO_4), thus avoiding the interaction between metal oxides and FePO_4 .³¹

Herein, amorphous FePO_4 as a support coupled with CePO_4 as an active component ($\text{CePO}_4/\text{FePO}_4$) still exhibits approximately 81% NO_x reduction activity with 6 wt % K_2O poisoning. The introduction of amorphous FePO_4 could break through the traditional antipotassium mechanism of the acid–base neutralization principle. The ultrahigh potassium storage capacity is attributed to the spontaneous migration of potassium into the bulk phase of amorphous FePO_4 within the NH_3 -SCR reaction temperature window. The self-adaptive bulk-phase alkali-tolerance strategy of the amorphous FePO_4 support provides a promising prospect for NO_x reduction under the poisoning scenario of ultrahigh alkali metal amounts.

MATERIALS AND METHODS

Catalyst Synthesis. An amorphous- FePO_4 -supported CePO_4 catalyst was obtained by the precipitation method. First, 5.350 g of $\text{Fe}(\text{NO}_3)_3\cdot9\text{H}_2\text{O}$ was dissolved in 200 mL of deionized water, and then, 1.152 mL of H_3PO_4 (molar ratio of P/Fe = 1.5) was added and stirred for 10 min, denoted as liquid A. 6.25 wt % of $\text{NH}_3\cdot\text{H}_2\text{O}$ was injected to liquid A dropwise, adjusting the pH to 2.2, which was recorded as suspension B. The required amount of $\text{Ce}(\text{NO}_3)_3\cdot6\text{H}_2\text{O}$ was measured and dissolved in 50 mL of deionized water. After the Ce solution was added to suspension B dropwise, the pH was adjusted to 6.0 with 6.25 wt % of $\text{NH}_3\cdot\text{H}_2\text{O}$, and the mixture was stirred for 1 h. The product was centrifuged and washed until pH = 7, and then dried in an oven at 100 °C. Finally, the precursor was calcined at 450 °C for 4 h in a tube furnace in static air with a ramp rate of 2 °C/min. The 25 wt % CePO_4 batch charge is denoted as $\text{CePO}_4/\text{FePO}_4$.

A commercial 1 wt % V_2O_5 -5 wt % WO_3/TiO_2 catalyst was synthesized with an impregnation method.⁵ 0.266 g of ammonium metatungstate and 0.064 g of NH_4VO_3 were dissolved in 100 mL of deionized water. Then, 5.000 g of TiO_2 synthesized with the hydrothermal method was measured and added to the solution. After magnetic stirring for 1 h, the suspension was dried on a rotary evaporator at 50 °C. Finally, the precursor was calcined at 500 °C for 4 h in a tube furnace

in static air with a ramp rate of 2 °C/min and is denoted as 1V5W/TiO₂.

Simulated Poisoning. The simulated poisoning process was achieved via impregnating catalysts with a KNO_3 solution. First, 1 g of $\text{CePO}_4/\text{FePO}_4$ or 1V5W/TiO₂ was dispersed in 15 mL of deionized water, and then, 5 mL of the required dissolved KNO_3 (calculated by the weight of K_2O) solution was added to the suspension and stirred for 1 h. After being dried in a 100 °C oven, the powder was calcined in a tube furnace at 450 °C for 4 h in static air with a ramp rate of 2 °C/min. The alkali-metal-poisoned catalysts are denoted as $\text{CePO}_4/\text{FePO}_4\text{-}x\text{K}$ or 1V5W/TiO₂-*x*K, where *x* represents the weight percentage of K_2O .

Catalytic Performance Evaluation. 0.3 g of catalyst within 40–60 mesh was loaded in the quartz tube with a 7 mm inner diameter. The feed gas was composed of 500 ppm of NO, 500 ppm of NH_3 , and 5% O_2 and balanced with N_2 to reach a total flow rate of 250 mL/min. The outlet of the flow was monitored by an FTIR detector (Protea AtmosFIR). The NO_x conversion and N_2 selectivity were calculated by the following formulas

$$\text{NO}_x \text{ conversion (\%)} = \frac{[\text{NO}_x]_{\text{in}} - [\text{NO}_x]_{\text{out}}}{[\text{NO}_x]_{\text{in}}} \quad (1)$$

$$\text{N}_2 \text{ selectivity (\%)} = \left(1 - \frac{2[\text{N}_2\text{O}]_{\text{out}}}{[\text{NO}_x]_{\text{in}} + [\text{NH}_3]_{\text{in}} - [\text{NO}_x]_{\text{out}} - [\text{NH}_3]_{\text{out}}} \right) \quad (2)$$

where NO_x represents NO and NO_2 . $[\text{NO}_x]_{\text{in}}$, $[\text{NO}_x]_{\text{out}}$, $[\text{N}_2\text{O}]_{\text{out}}$, $[\text{NH}_3]_{\text{in}}$, and $[\text{NH}_3]_{\text{out}}$ represent the inlet and outlet gas concentrations, respectively.

The WHSV was calculated by the following formula:

$$\text{WHSV} = \frac{q_v}{w} \quad (3)$$

q_v and w represent the total flow rate and the weight of catalysts, respectively. The activation energy was measured below 20% NO_x conversion with 0.15 g of catalyst and 200 000 $\text{mL}\cdot\text{g}^{-1}\cdot\text{h}^{-1}$ WHSV.

The other characterization methods are listed in the Supporting Information in detail.

RESULTS AND DISCUSSION

Catalytic Performance. The optimal batch charge of CePO_4 was determined to be 25 wt % of FePO_4 by investigating different loading amounts of CePO_4 with and without K_2O poisoning (Figures S1 and S2). Therefore, the 25 wt % $\text{CePO}_4/\text{FePO}_4$ (denoted as $\text{CePO}_4/\text{FePO}_4$) catalyst was selected to explore catalytic activity and the antipoisoning mechanism under different amounts of alkali metal poisoning. Compared with TiO_2 and CeO_2 , which are traditional NH_3 -SCR catalyst supports, the 3 wt % K_2O poisoning dramatically deactivated the 25 wt % $\text{CePO}_4/\text{TiO}_2$ and 25 wt % $\text{CePO}_4/\text{CeO}_2$ catalysts, indicating that the common TiO_2 and CeO_2 were unable to provide high alkali resistance (Figure S3). Considering thermostability and the existence of O_2 , the majority of potassium-ion battery materials were not suitable to be applied as NH_3 -SCR catalyst supports, but the conversion-type material such as amorphous FeVO_4 and the intercalation-type material such as $\text{K}_x\text{Ti}_2\text{O}_9$ and K_xMnO_2 were

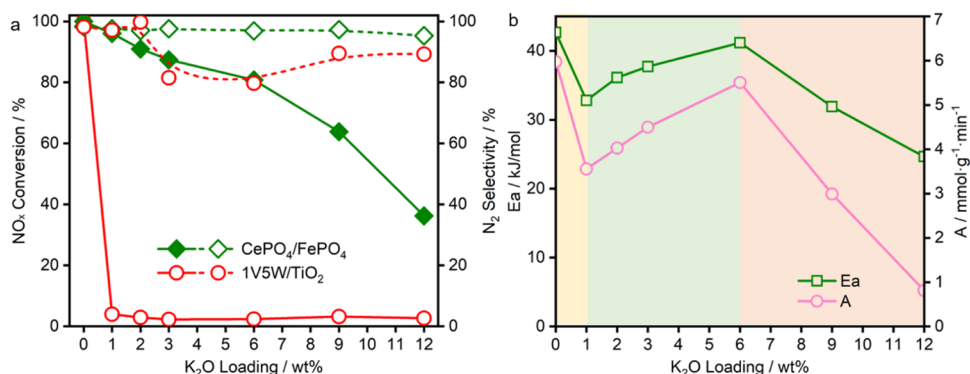


Figure 1. (a) NO_x conversion (solid line) and N₂ selectivity (dashed line) of the CePO₄/FePO₄ and commercial 1V5W/TiO₂ catalysts as a function of K₂O loading amount. Reaction conditions: [NO] = [NH₃] = 500 ppm, [O₂] = 5%, N₂ as the balance gas, total flow rate of 250 mL/min, and WHSV = 50 000 mL·g⁻¹·h⁻¹. (b) Activation energy (E_a) and pre-exponential factor (A) of CePO₄/FePO₄ as a function of K₂O loading amount. Reaction conditions: [NO] = [NH₃] = 500 ppm, [O₂] = 5%, N₂ as the balance gas, total flow rate of 500 mL/min, and WHSV = 200 000 mL·g⁻¹·h⁻¹.

synthesized in air and high-temperature conditions, which could be employed as catalysts or supports.³² However, when CePO₄ was supported on them, according to the SCR performance evaluation of catalysts with 3 wt % K₂O poisoning, amorphous FeVO₄ and K_xTi₂O₉ exhibited poor alkali resistance, while K_xMnO₂ exhibited poor N₂ selectivity and a narrow temperature window, implying that they were unaccommodated for alkali-resistant NH₃–SCR catalyst design (Figure S4).

As shown in Figures 1a, S5, and S6, when merely 1 wt % of K₂O existed on the commercial catalyst 1V5W/TiO₂ at 360 °C, the catalyst was completely deactivated. However, when amorphous FePO₄ was applied as the support, the activity of the CePO₄/FePO₄ catalyst at 360 °C only decreased by 3.9 and 12.6% under 1 and 3 wt % K₂O poisoning, respectively. Even at the poisoning amounts of up to 6 wt % K₂O, CePO₄/FePO₄ could still maintain 81% NO_x conversion at 360 °C. When the K₂O poisoning amounts reached 12 wt %, CePO₄/FePO₄ still remained 36% NO_x abatement efficiency, implying that amorphous FePO₄ exhibited extraordinary alkali metal resistance. Besides, with the poisoning of K₂O, the N₂ selectivity of the commercial 1V5W/TiO₂ catalyst showed an obvious decrease, but the N₂ selectivity of CePO₄/FePO₄ exhibited more than 95% under 0–12 wt % K₂O poisoning.

According to the results of the reaction kinetics test (Figures 1b and S7), the apparent activation energy (denoted as E_a) of CePO₄/FePO₄ decreased from 42.66 to 32.81 kJ/mol after being poisoned by 1 wt % of K₂O. Based on previous reports of alkali metal poisoning in NH₃–SCR, the electron-donating effect of alkali metals usually caused the decrease of activation energy.³³ However, alkali metals occupied a large number of NH₃ adsorption sites, which was also found from the decline of the pre-exponential factor (denoted as A).³³ Due to the stronger competitive adsorption effect than the electron-donating effect, the apparent activity induced by alkali metals was normally dramatically decreased.⁹ However, in this study, when the amount of K₂O was increased to 2 wt %–6 wt %, both the apparent activation energy and the pre-exponential factor showed a monotonous promotion, indicating that the amorphous FePO₄ support could store vast amounts of K₂O and simultaneously generate new species, thereby retarding the rapid deactivation. When the amount of K₂O was further elevated to 9–12 wt %, the E_a, A, and catalytic performance of the catalysts decreased sharply again, elucidating that super-

fluous K₂O might not be effectively stored by the amorphous FePO₄ support and could poison CePO₄ and the newly generated species. Although the NO_x abatement efficiency of CePO₄ was excellent, it was severely poisoned by 3 wt % of K₂O, indicating that the alkali resistance was not provided by CePO₄ (Figure S8). We assumed that the newly generated species was Fe₂O₃, which could be formed during the reaction between FePO₄ and K₂O, while the 6.8 wt % Fe₂O₃/FePO₄ (equivalently to the amount of Fe₂O₃ formed during the reaction between FePO₄ and 12 wt % of K₂O) only showed the topmost NO_x conversion less than 60% (Figure S8), while the topmost NO_x conversion of CePO₄/FePO₄ was higher than 60% even under 9 wt % K₂O poisoning. The much inferior NO_x conversion of 6.8 wt % Fe₂O₃/FePO₄ compared to CePO₄/FePO₄ elucidated that the active sites were still CePO₄ not formed Fe₂O₃ after K₂O poisoning.

Besides, amorphous FePO₄ also exhibited excellent resistance to Na₂O, PbO, CaO, and CdO (Figures S9–S11). The topmost NO_x conversion of CePO₄/FePO₄ still retain 75% at 50 000 mL·g⁻¹·h⁻¹ WHSV under the coexistence of 3 wt % of K₂O, 3 wt % of Na₂O, 3 wt % of PbO, 3 wt % of CaO, and 3 wt % of CdO, leading to a flexible application for the working conditions containing alkali, alkali earth, and heavy metals in flue gas. In the long-time stability test in the simulated NH₃–SCR stream, the catalytic performance of CePO₄/FePO₄ was kept higher than 95%, while in the simulated NH₃–SCR stream with H₂O and SO₂, the catalytic performance of CePO₄/FePO₄ was kept higher than 85% and recovered to 96% when H₂O and SO₂ were cut off (Figure S12). According to the XRD pattern of the samples after a long-time stability test, the structure of CePO₄ was unchanged and FePO₄ still remained amorphous, without other species observed on the XRD pattern (Figure S13).

Considering the diffusion limitation of potassium ions in crystal FePO₄ for potassium-ion batteries, the alkali resistance of crystal FePO₄ was also evaluated and the alkali resistance was inferior to that of amorphous FePO₄ (Figure S14). Furthermore, the 3 wt % K₂O resistance on common amorphous supports for NH₃–SCR catalysts, such as Ce_{0.3}TiO_x and TiZrO_x, was also conducted and the alkali resistances were both superior to those of crystal CeO₂ and TiO₂ supports (Figure S15). Therefore, an amorphous structure was vital for outstanding alkali tolerance because the dense lattice structure of the crystal might hinder the

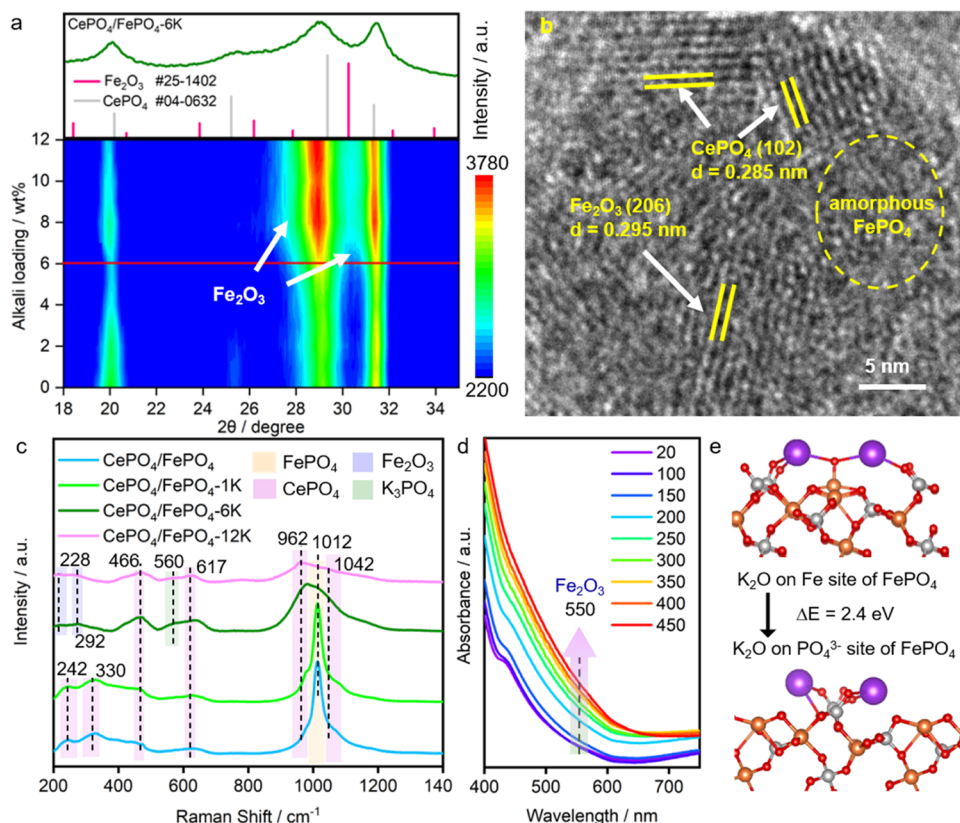


Figure 2. (a) XRD patterns of CePO₄/FePO₄ under 0–12 wt % K₂O poisoning after being calcined at 450 °C; (b) high-resolution TEM image of CePO₄/FePO₄-6K; (c) Raman spectra of CePO₄/FePO₄ under 0–12 wt % K₂O poisoning after being calcined at 550 °C; (d) *in situ* UV–vis diffuse reflectance spectra of CePO₄/FePO₄ under 12 wt % K₂O poisoning without following calcination; (e) energy difference between K₂O on Fe and PO₄³⁻ sites of FePO₄.

diffusion of alkali metal into the bulk phase under thermocatalytic conditions.

Phosphate Species Evolution for Alkali Resistance. In order to understand the excellent alkali metal resistance mechanism of amorphous FePO₄, the structural features were investigated using XRD, high-resolution TEM, Raman spectra, and UV–vis diffuse reflectance spectra (UV–vis DRS). Figure 2a shows the XRD patterns of CePO₄/FePO₄ catalysts with various loading amounts of K₂O. The (101) and (102) crystal plane intensities of CePO₄ (PDF# 04-0632) at 20.17 and 31.36° gradually decreased with the increment of K₂O from 0 to 6 wt %, indicating the decline of the surface CePO₄ phase and the generation of new species with K₂O added. When the K₂O loading was further increased, new species could be notably observed at 27.86 and 30.27°, which was assigned to the fingerprint feature of Fe₂O₃ (PDF# 25-1402). The new species Fe₂O₃ might be originated from the solid-phase reaction between FePO₄ and potassium.³⁴ To intensively verify the existence of Fe₂O₃, highly crystalline Fe₂O₃ could be distinctly identified at $2\theta = 20.69^\circ$ via increasing the calcination temperature of the poisoned catalyst to 550 °C (Figure S16). High-resolution TEM was further applied to demonstrate the existence of Fe₂O₃ again. Fe₂O₃ with a lattice spacing of 0.295 nm, attributed to the (206) facet, is clearly found in Figure 2b. Besides, amorphous FePO₄ and crystal CePO₄ with the (102) facet are also observed in Figures 2b and S17, respectively. Furthermore, the existence of Fe₂O₃ was also confirmed by Raman spectra. As shown in Figure S18, when K₂O-poisoned CePO₄/FePO₄ was calcined at 450 °C,

only amorphous FePO₄ was observed at 1003 cm⁻¹, and Fe₂O₃ displayed a negligible Raman signal.^{35,36} To fortify the Raman intensity of Fe₂O₃, CePO₄/FePO₄ was calcined at 550 °C and then notable Raman peaks of Fe₂O₃ could be detected at 228 and 292 cm⁻¹ under more than 6 wt % K₂O poisoning in Figure 2c. Besides, new species K₃PO₄ at 560 cm⁻¹ was also visible, but FePO₄ at 330 and 1012 cm⁻¹ basically disappeared, indicating that FePO₄ could capture K₂O to form Fe₂O₃ and K₃PO₄.^{36–39} When CePO₄/FePO₄ was poisoned by K₂O, the observation of H₂-TPR signals assigned to Fe₂O₃ reduction also proved the existence of Fe₂O₃ (Figure S19).

In order to disclose the onset temperature of the solid-phase reaction between FePO₄ and potassium, *in situ* UV–vis DRS of CePO₄/FePO₄ under 12 wt % K₂O poisoning without following calcination is displayed in Figure 2d. UV–vis diffuse reflectance spectra of CePO₄/FePO₄ under 0–12 wt % K₂O poisoning followed by calcining at 450 °C also proved the existence of Fe₂O₃ indeed (Figure S20) because the intensity of the characteristic peak at 550 nm (ascribed to Fe₂O₃) was gradually increased with the augment of alkali metal loading amounts, and meanwhile, catalyst colors changed from light yellow to wheat (Figure S21).¹⁶ When the treatment temperature increased to 150 °C, the characteristic absorbance of Fe₂O₃ at 550 nm started to become apparent. This suggested that the solid-phase reaction could be impelled to generate Fe₂O₃ as long as the reaction temperature was above 150 °C, which matched with the conventional NH₃–SCR temperature window.^{13,40} Besides, the energy difference between K₂O on Fe and PO₄³⁻ sites of FePO₄ was also

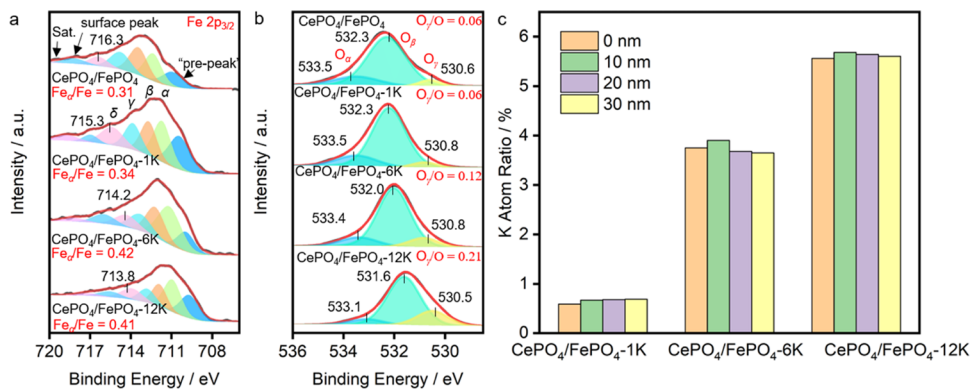


Figure 3. (a) Fe 2p_{3/2} and (b) O 1s XPS spectra and (c) calculated potassium atom ratio at 0–30 nm etching depth on CePO₄/FePO₄ with 0–12 wt % K₂O poisoning.

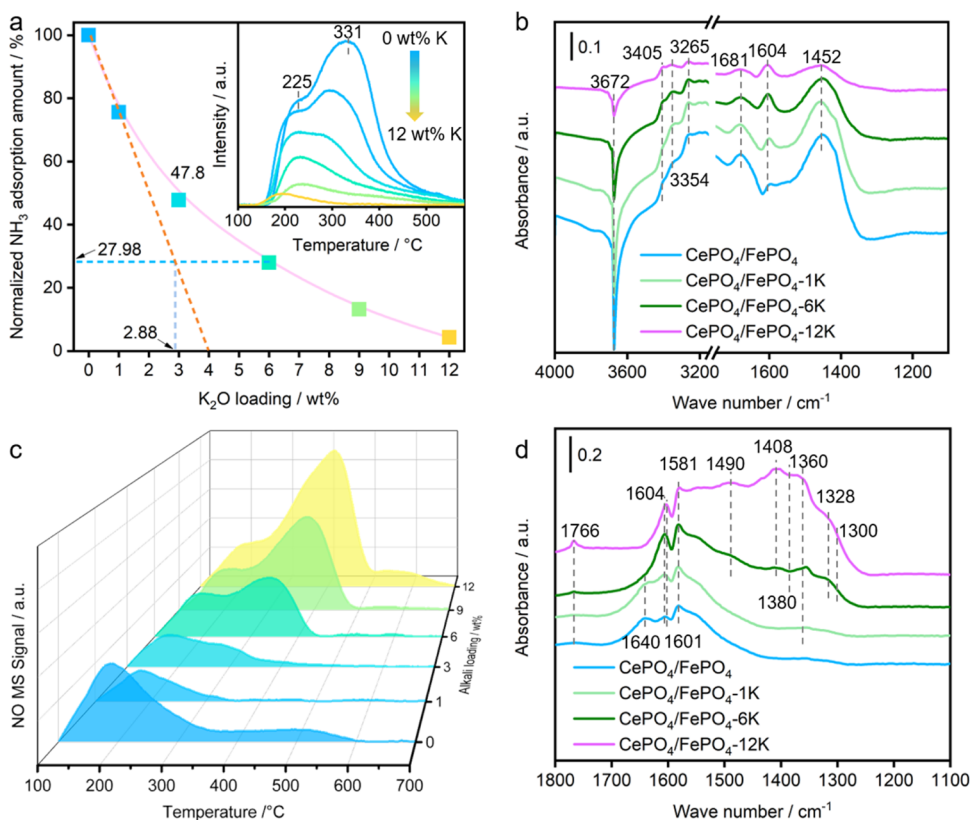


Figure 4. (a) Normalized NH₃ adsorption amounts of CePO₄/FePO₄ catalysts in NH₃-TPD-MS (inset shows the mass spectral signal of NH₃); (b) in situ DRIFTS of adsorbed NH₃ at 50 °C; (c) the mass spectral signal of NO in NO + O₂-TPD-MS; (d) in situ DRIFTS of adsorbed NO_x at 50 °C for CePO₄/FePO₄ with 0–12 wt % K₂O poisoning.

investigated via DFT calculation (Figure 2e), and K₂O was spontaneously combined with FePO₄ (Table S1) and tended to bind on the PO₄³⁻ site since the energy of K₂O on PO₄³⁻ sites is 2.4 eV lower than that of K₂O on Fe sites.

In order to further unveil the phosphate species evolution, Fe 2p_{3/2} and O 1s of XPS spectra were characterized and are exhibited in Figures 3a and 3b, respectively. The high-spin Fe 2p_{3/2} envelope was fitted as 6 peaks, which were “pre-peak”, α , β , γ , δ , and surface peak with the increase of binding energy.⁴¹ The binding energy of the Fe 2p_{3/2} δ peak was gradually decreased from 716.3 to 713.8 eV with an increase in K₂O amounts from 0 wt % to 12 wt %. The decline of binding energy was ascribed to the lower electronegativity of Fe than P, suggesting the coordination environment variation from Fe–

O–P to Fe–O–Fe and the species evolution from FePO₄ to Fe₂O₃. Moreover, the low-binding energy Fe 2p_{3/2} α peak area also increased from 0.31 to 0.41 with the increase of the K₂O poisoning amount, proving the increase of Fe₂O₃. When Fe was transformed from FePO₄ to Fe₂O₃, phosphate could combine with potassium. The monotonously decreased binding energy of the P element implied the coordination environment of P–O–Fe altered to P–O–K (Figure S22).

As shown in Figure 3c, the O _{α} (533.1–533.5 eV), O _{β} (531.6–532.3 eV), and O _{γ} (530.5–530.6 eV) were assigned to O species in hydroxyl groups, PO₄³⁻, and Fe₂O₃, respectively.⁴² With an increase in K₂O amounts, the ratio of O _{γ} /O_{total} was notably increased from 0.06 to 0.21, indicating the buildup of Fe₂O₃. The binding energy of Ce³⁺ 3d_{5/2}

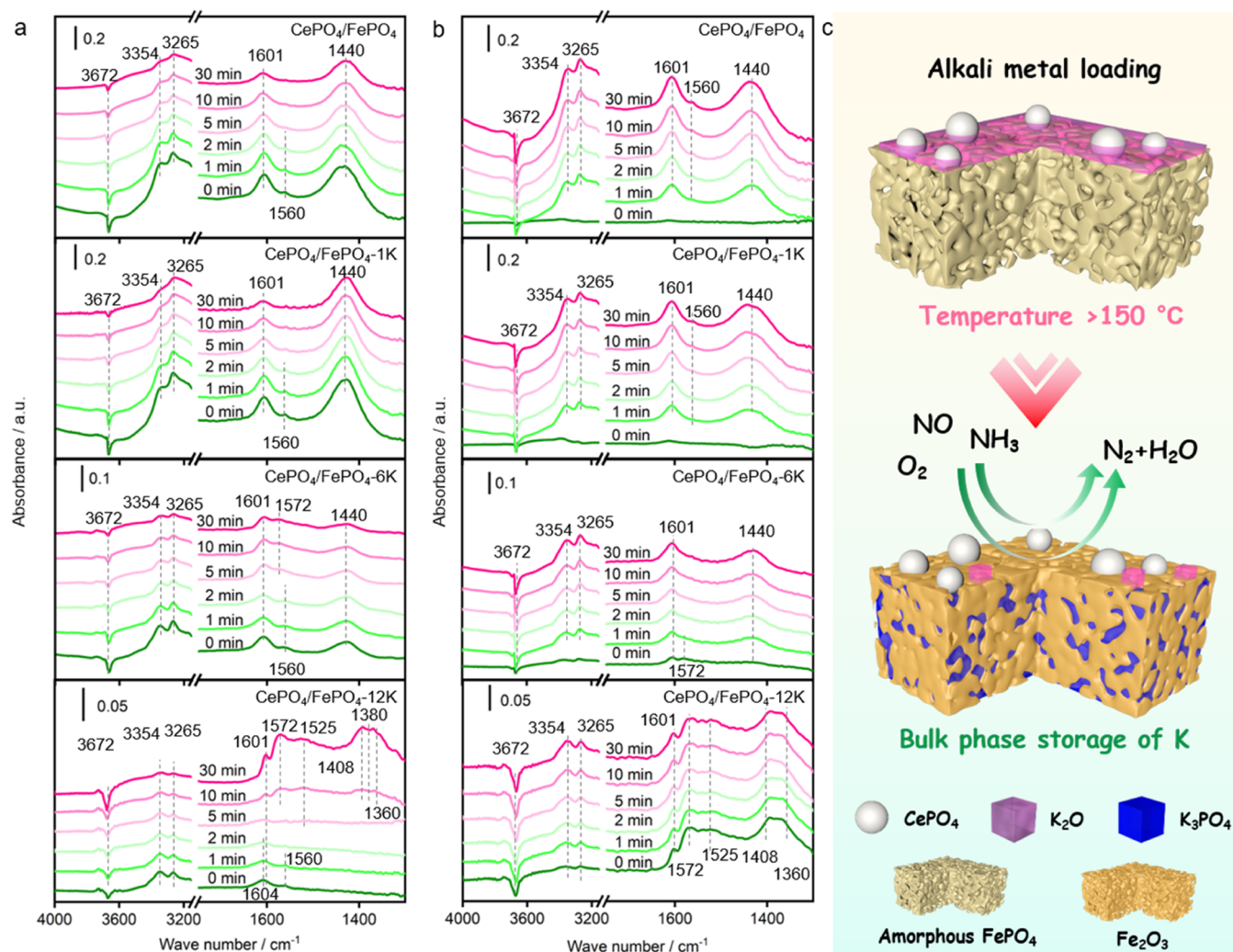


Figure 5. (a) *In situ* DRIFTS of preadsorbed NH₃ with gaseous NO + O₂ and (b) *in situ* DRIFTS of preadsorbed NO_x with gaseous NH₃ transition reaction for CePO₄/FePO₄ with 0–12 wt % K₂O poisoning at 240 °C. Reaction condition: [NH₃] = 1000 ppm, [NO] = 1000 ppm, [O₂] = 5%, carrier gas was N₂. (c) Schematic diagram of self-adaptive bulk-phase storage of K₂O in amorphous FePO₄.

remained relatively unchanged due to the protection of FePO₄ until the K₂O amounts exceeded 6 wt % (Figure S23). When the K₂O amounts were further increased to 12 wt %, the binding energy of Ce³⁺ 3d_{5/2} was decreased, implying the combination of Ce and excess potassium species.

To ascertain the K₂O diffusion position (bulk phase or surface) in amorphous FePO₄, the potassium atom ratio at different etching depths in the range of 0–30 nm for CePO₄/FePO₄ with 1, 6, and 12 wt % K₂O poisoning amounts is exhibited in Figure 3c. Independent of etching depth, the average potassium atomic ratio was all maintained at approximately 0.7, 3.8, and 5.6% when K₂O amounts were 1, 6, and 12 wt %, respectively, manifesting the highly uniform distribution of K₂O in the bulk phase of amorphous FePO₄.

Chemisorption Behavior Variation during Alkali Poisoning. NH₃-TPD-MS was used to demonstrate the variation of surface acid quantity induced by K₂O poisoning in Figure 4a.^{43–45} As shown in the inset of Figure 4a, two obvious NH₃ desorption peaks at 225 and 331 °C for fresh CePO₄/FePO₄ catalysts could be classified as medium and strong acid sites, respectively.⁴⁶ Surface acid quantity could be reflected via normalized NH₃ adsorption amounts. It can be found that surface-adsorbed NH₃ gradually decreased with K₂O increase-

ment. It was generally considered that the low amount of K₂O (e.g., 1 wt %) was only bound with surface acid sites. Based on this hypothesis, we inferred that the surface acid sites on CePO₄/FePO₄ catalysts would be completely consumed when K₂O poisoning amounts were about 4 wt %. However, even when K₂O poisoning amounts were 6 wt %, CePO₄/FePO₄ catalysts still possessed considerable surface acid quantity (28%) and displayed 81% NO_x purification efficiency, implying that K₂O was not just captured by surface acid sites but might migrate into the bulk phase of the support. In order to further verify the migration mechanism, EDS was applied to detect surface potassium distribution and content. The results showed that the content of well-distributed potassium on the surface was significantly lower than the actual loading amounts (Figures S24–S29).

To identify the types and thermal stabilities of surface acid sites for CePO₄/FePO₄ catalysts poisoned by 0–12 wt % of K₂O, the infrared spectra of NH₃ adsorption at 50 °C are displayed in Figure 4b.⁴⁷ The peaks at 1452 and 1681 cm⁻¹ were both assigned to NH₄⁺ species adsorbed on Brønsted acid sites (denoted as B-NH₄⁺).⁴⁸ The peaks at 1604, 3265, 3354, and 3405 cm⁻¹ were all attributed to NH₃ species adsorbed on Lewis acid sites (denoted as L-NH₃).^{49,50} The Brønsted acid

sites on the surface showed a rapid decline after K₂O poisoning, which might be a result of the K₂O preferential binding to Brønsted acid sites. Moreover, nitrogen isothermal adsorption tests also revealed that the decline of specific surface area was slight in the range of 1–9 wt % K₂O poisoning (Figure S30), excluding the influence of physics coverage. According to the *in situ* DRIFTS of NH₃ desorption in Figures S31–S34, the L-NH₃ and B-NH₄⁺ on the fresh CePO₄/FePO₄ barely desorbed at 250 °C, but the L-NH₃ and B-NH₄⁺ on the surface were almost completely desorbed at 250 °C on CePO₄/FePO₄-6K and at 200 °C on CePO₄/FePO₄-12K, indicating that the thermally stable acid sites were gradually occupied with the increase of K₂O.

The chemisorption of NO was also investigated by NO + O₂-TPD-MS and *in situ* DRIFTS. As shown in Figure 4c, the adsorption amounts of NO decreased when poisoned with 1 wt % of K₂O because alkali metals can weaken the adsorption energy of NO.⁵¹ However, when the K₂O loading amounts increased to 3–12 wt %, the adsorption amount of NO enhanced significantly and the desorption temperature moved to high temperatures, demonstrating that new sites with intense NO adsorption might be generated in the poisoning process. Combined with the structure evolution of amorphous FePO₄ against K₂O poisoning, Fe₂O₃ and its interaction with alkali metals may be responsible for the intense adsorption of NO. Therefore, *in situ* DRIFTS of NO + O₂ desorption were obtained (Figures S35–S38), and the *in situ* DRIFTS of adsorbed NO_x at 50 °C are displayed in Figure 4d. The peaks at 1300 and 1581 cm⁻¹ were both attributed to bidentate nitrate. The peaks at 1328, 1360, and 1408 cm⁻¹ were all attributed to nitrite, and the peaks from 1380 cm⁻¹ were attributed to NO₃⁻.⁵² The peaks at 1490–1525, 1601, 1604–1640, and 1766 cm⁻¹ were attributed to monodentate nitrate, adsorbed NO₂, bridge nitrate, and N₂O₄ species, respectively.⁵³ At 50 °C, the surface NO_x species observed on the CePO₄/FePO₄ catalyst were mainly composed of bridge nitrate, bidentate nitrate, and nitrite. The adsorption form of the NO_x barely changed when CePO₄/FePO₄ was just poisoned with 1 wt % of K₂O. However, the peak intensities of bidentate nitrate, monodentate nitrate, NO₃⁻, NO₂, and N₂O₄ were significantly enhanced as alkali metal poisoning reached 6 and 12 wt %, resembling the *in situ* DRIFTS of adsorbed NO + O₂ on the K-poisoned Fe₂O₃/TiO₂ catalyst in Zhang et al.'s work.⁵⁴ When K₂O loading amounts exceeded 6 wt %, those K₂O-induced nitrates were thermally stable nitrates because they barely decomposed on K₂O-poisoned CePO₄/FePO₄ even when the temperature was elevated to 250 °C (Figures S37 and S38), indicating that the thermally stable nitrates would accumulate on the catalyst surface and might give rise to a rapid deactivation.

Adaptive Alkali Metal Resistance Mechanism. In order to explore the effect of self-adaptive bulk-phase storage of K₂O in amorphous FePO₄ on the NH₃-SCR reaction mechanism, *in situ* DRIFTS of transient reaction for CePO₄/FePO₄ with 0–12 wt % K₂O poisoning were obtained at 240 °C. As shown in Figure 5a, NH₃ could be effectively adsorbed on Lewis acid (1560, 1601, 3265, and 3354 cm⁻¹) and Brønsted acid (1440 cm⁻¹) sites over CePO₄/FePO₄.⁵⁵ With the introduction of NO + O₂, L-NH₃ and B-NH₄⁺ reacted with NO, and the reaction rate of L-NH₃ was faster than that of B-NH₄⁺ (Figure S39) on CePO₄/FePO₄ and CePO₄/FePO₄-1K.⁵⁶

When the amount of K₂O poisoning increased to 6 wt %, the proportion of L-NH₃ was higher than that of B-NH₄⁺ at 240

°C, implying that Brønsted acid sites were preferentially occupied by K₂O on CePO₄/FePO₄-6K. Fortunately, according to the intensity decline at 3265 and 3354 cm⁻¹, remaining L-NH₃ was still able to react with gaseous NO. Therefore, after NO + O₂ was injected for 2 min, the enlarged infrared peaks at 1572 and 1601 cm⁻¹ should be ascribed to the formation of bridge nitrate, indicating that nitrates started to accumulate on CePO₄/FePO₄-6K. As can be seen from Figure 5b, after NO + O₂ was preadsorbed for 1 h on CePO₄/FePO₄ and CePO₄/FePO₄-1K, there was basically no infrared peak of NO_x species on the catalyst surface. Combined with the results of NO_x-TPD and *in situ* DRIFTS of NO + O₂ desorption in Figures 4c, S35, and S36, NO_x adsorption on CePO₄/FePO₄ and CePO₄/FePO₄-1K was pretty weak at 240 °C. Because CePO₄/FePO₄ could not effectively adsorb nitrates under 240 °C while Fe₂O₃ showed strong absorption of nitrates (Figure 4d), the additional nitrates adsorbed on CePO₄/FePO₄-6K compared to CePO₄/FePO₄ also proved that Fe₂O₃ yielded in the process of K₂O capture.

When the amount of K₂O poisoning increased to 12 wt %, B-NH₄⁺ was barely noticeable from the infrared spectrum in Figure 5a, showing that the Brønsted acid sites on CePO₄/FePO₄-12K were primarily covered by K₂O. After 5 min, the infrared peaks of nitrite (1360, 1408 cm⁻¹), NO₃⁻ (1380 cm⁻¹), and monodentate nitrate (1525 cm⁻¹) appeared on the surface of CePO₄/FePO₄-12K, which were ascribed to the nitrite and nitrates species on K₂O-poisoned Fe₂O₃ based on the results of *in situ* DRIFTS of NO + O₂ desorption (Figures 4d and S38), also indicating that K₂O was captured by amorphous FePO₄. Under the condition of K₂O fixing into the bulk phase of amorphous FePO₄ and rapid consumption of Brønsted acid sites, although the intensity of L-NH₃ (3265 and 3354 cm⁻¹) was also very weak, it could still react with gaseous NO in 30 min, which should be a reason for residual NO_x reduction performance under extremely high K₂O poisoning amounts. According to Figure 5b, after preadsorption of NO + O₂ on CePO₄/FePO₄-12K, the adsorbed nitrates and nitrite were barely reacted with gaseous NH₃ at 240 °C. Therefore, the dramatically decreased acid sites and gradually accumulated inert nitrate species displayed rapid deactivation when the amount of K₂O exceeded the storage threshold (ca. 6 wt %).

As demonstrated in Figure 5c, the ultrahigh K₂O resistance capacity of amorphous FePO₄ was derived from two aspects. On the one hand, CePO₄/FePO₄ possesses abundant acid contents, which can capture a part of K₂O. On the other hand, K₂O can spontaneously migrate into the bulk phase of amorphous FePO₄ and be anchored in the form of K₃PO₄ within the NH₃-SCR reaction temperature window (above 150 °C), which is accompanied by Fe₂O₃ generation. In the practical operation condition, the gradually accumulated alkali metals would be automatically reacted with the amorphous FePO₄ support under working conditions, exhibiting self-adaptive alkali tolerance and endowing the catalysts with ultrahigh alkali metal resistance.

ENVIRONMENTAL IMPLICATIONS

With the employment of amorphous FePO₄ as the catalyst support, an ultrahigh alkali metal resistance capacity greater than that of 6 wt % of K₂O was achieved via bulk-phase storing poison. Even when the K₂O poisoning amounts are elevated up to 12 wt %, 36% NO_x abatement efficiency still remains. Besides, amorphous FePO₄ also exhibited excellent resistance

to Na₂O, PbO, CaO, CdO, H₂O, and SO₂, leading to a flexible application for the working conditions containing alkali and heavy metals in flue gas. The cheap and available amorphous FePO₄ provides a long-durability NH₃-SCR catalyst to save the cost of frequently replacing and regenerating the catalyst, providing a wide prospect for alkali/heavy-metal-durability catalyst designing. This strategy breaks through the traditional acid-base neutralization concept for alkali resistance in NH₃-SCR catalyst designing and provides a solution for the ultralow emission of NO_x in coal-fired power plants, waste incineration furnaces, biomass fuels, and other NO_x emission sources containing alkali and heavy metals.

ASSOCIATED CONTENT

Supporting Information

The Supporting Information is available free of charge at <https://pubs.acs.org/doi/10.1021/acs.est.3c05112>.

Information about reagents and materials; morphology and structure characterization; chemical adsorption characterization; *in situ* DRIFTS study; selective catalytic reduction of NO_x (Figures S1–S6, S8–S12, S14, and S15); Arrhenius plots (Figure S7); XRD patterns (Figures S13 and S16); HR TEM (Figure S17); Raman spectra (Figure S18); H₂-TPR profiles (Figure S19); UV-vis DRS (Figure S20); optical photograph of alkali-poisoned CePO₄/FePO₄ (Figure S21); XPS spectra (Figures S22 and S23); EDS mapping (Figures S24–S27); EDS results (Figure S28); the gap between the surface K₂O amount and loading amount (Figure S29); BET surface area (Figure S30); *in situ* DRIFTS (Figures S31–S38); normalized reaction rates of adsorbed B-NH₄⁺ and L-NH₃ (Figure S39) ([PDF](#))

AUTHOR INFORMATION

Corresponding Author

Dengsong Zhang — State Key Laboratory of Advanced Special Steel, School of Materials Science and Engineering, International Joint Laboratory of Catalytic Chemistry, College of Sciences, Shanghai University, Shanghai 200444, China; orcid.org/0000-0003-4280-0068; Email: dszhang@shu.edu.cn

Authors

Zhi Shen — State Key Laboratory of Advanced Special Steel, School of Materials Science and Engineering, International Joint Laboratory of Catalytic Chemistry, College of Sciences, Shanghai University, Shanghai 200444, China

Penglui Wang — State Key Laboratory of Advanced Special Steel, School of Materials Science and Engineering, International Joint Laboratory of Catalytic Chemistry, College of Sciences, Shanghai University, Shanghai 200444, China

Xiaonan Hu — State Key Laboratory of Advanced Special Steel, School of Materials Science and Engineering, International Joint Laboratory of Catalytic Chemistry, College of Sciences, Shanghai University, Shanghai 200444, China

Wenqiang Qu — State Key Laboratory of Advanced Special Steel, School of Materials Science and Engineering, International Joint Laboratory of Catalytic Chemistry, College of Sciences, Shanghai University, Shanghai 200444, China

Xiangyu Liu — State Key Laboratory of Advanced Special Steel, School of Materials Science and Engineering, International Joint Laboratory of Catalytic Chemistry, College of Sciences, Shanghai University, Shanghai 200444, China

Complete contact information is available at: <https://pubs.acs.org/10.1021/acs.est.3c05112>

Notes

The authors declare no competing financial interest.

ACKNOWLEDGMENTS

This work was financially supported by the National Natural Science Foundation of China (22125604).

REFERENCES

- (1) Kaufman, J. D.; Adar, S. D.; Barr, R. G.; Budoff, M.; Burke, G. L.; Curl, C. L.; Daviglus, M. L.; Roux, A. V. D.; Gassett, A. J.; Jacobs, D. R.; Kronmal, R.; Larson, T. V.; Navas-Acien, A.; Olives, C.; Sampson, P. D.; Sheppard, L.; Siscovick, D. S.; Stein, J. H.; Szpiro, A. A.; Watson, K. E. Association between air pollution and coronary artery calcification within six metropolitan areas in the USA (the Multi-Ethnic Study of Atherosclerosis and Air Pollution): a longitudinal cohort study. *Lancet* **2016**, *388*, 696–704.
- (2) Anenberg, S. C.; Miller, J.; Minjares, R.; Du, L.; Henze, D. K.; Lacey, F.; Malley, C. S.; Emberson, L.; Franco, V.; Klimont, Z.; Heyes, C. Impacts and mitigation of excess diesel-related NO_x emissions in 11 major vehicle markets. *Nature* **2017**, *545*, 467–471.
- (3) Li, J.; Han, X.; Zhang, X.; Sheveleva, A. M.; Cheng, Y.; Tuna, F.; McInnes, E. J. L.; McCormick McPherson, L. J.; Teat, S. J.; Daemen, L. L.; Ramirez-Cuesta, A. J.; Schröder, M.; Yang, S. Capture of nitrogen dioxide and conversion to nitric acid in a porous metal–organic framework. *Nat. Chem.* **2019**, *11*, 1085–1090.
- (4) Chen, W.; Zou, R.; Wang, X. Toward an atomic-level understanding of the catalytic mechanism of selective catalytic reduction of NO_x with NH₃. *ACS Catal.* **2022**, *12*, 14347–14375.
- (5) Lai, J.-K.; Wachs, I. E. A perspective on the selective catalytic reduction (SCR) of NO with NH₃ by supported V₂O₅-WO₃/TiO₂ catalysts. *ACS Catal.* **2018**, *8*, 6537–6551.
- (6) Hao, Z.; Shen, Z.; Li, Y.; Wang, H.; Zheng, L.; Wang, R.; Liu, G.; Zhan, S. The role of alkali metal in α-MnO₂ catalyzed ammonia-selective catalysis. *Angew. Chem., Int. Ed.* **2019**, *58*, 6351–6356.
- (7) Wang, W.; McCool, G.; Kapur, N.; Yuan, G.; Shan, B.; Nguyen, M.; Graham, U. M.; Davis, B. H.; Jacobs, G.; Cho, K.; Hao, X. K. Mixed-phase oxide catalyst based on Mn-Mullite (Sm, Gd)Mn₂O₅ for NO oxidation in diesel exhaust. *Science* **2012**, *337*, 832–835.
- (8) Zhang, H.; Kong, M.; Cai, Z.; Jiang, L.; Liu, Q.; Yang, J.; Ren, S.; Li, J.; Duan, M. Synergistic effect of arsenic and different potassium species on V₂O₅-WO₃/TiO₂ catalyst poisoning: Comparison of Cl⁻, SO₄²⁻ and NO₃⁻ anions. *Catal. Commun.* **2020**, *144*, No. 106069.
- (9) Wu, P.; Tang, X.; He, Z.; Liu, Y.; Wang, Z. Alkali metal poisoning and regeneration of selective catalytic reduction denitrification catalysts: Recent advances and future perspectives. *Energy Fuel* **2022**, *36*, S622–S646.
- (10) Wu, Q.; Han, L.; Li, S.; Wang, S.; Cong, Y.; Liu, K.; Lei, Y.; Zheng, H.; Li, G.; Cai, B.; Hao, J. Facility-level emissions and synergistic control of energy-related air pollutants and carbon dioxide in China. *Environ. Sci. Technol.* **2023**, *57*, 4504–4512.
- (11) Zhu, H.; Song, L.; Li, K.; Wu, R.; Qiu, W.; He, H. Low-temperature SCR catalyst development and industrial applications in China. *Catalysts* **2022**, *12*, 341.
- (12) Putluru, S. S. R.; Jensen, A. D.; Riisager, A.; Fehrmann, R. Heteropoly acid promoted V₂O₅/TiO₂ catalysts for NO abatement with ammonia in alkali containing flue gases. *Catal. Sci. Technol.* **2011**, *1*, 631–637.
- (13) Zhang, P.; Wang, P.; Impeng, S.; Lan, T.; Liu, X.; Zhang, D. Unique Compensation Effects of Heavy Metals and Phosphorus

- Copoisoning over NO_x Reduction Catalysts. *Environ. Sci. Technol.* **2022**, *S6*, 12553–12562.
- (14) Yao, X.; Kang, K.; Cao, J.; Chen, L.; Luo, W.; Zhao, W.; Rong, J.; Chen, Y. Enhancing the denitrification performance and anti-K poisoning ability of CeO₂-TiO₂/P25 catalyst by H₂SO₄ pretreatment: Structure-activity relationship and mechanism study. *Appl. Catal., B* **2020**, *269*, No. 118808.
- (15) Chen, S.; Xie, R.; Liu, Z.; Ma, L.; Yan, N. Efficient NO_x reduction against alkali poisoning over a self-protection armor by fabricating surface Ce₂(SO₄)₃ species: Comparison to commercial vanadia catalysts. *Environ. Sci. Technol.* **2023**, *S7*, 2949–2957.
- (16) Li, Y.; Cai, S.; Wang, P.; Yan, T.; Zhang, J.; Zhang, D. Improved NO_x reduction over phosphate-modified Fe₂O₃/TiO₂ catalysts via tailoring reaction paths by *in situ* creating alkali-poisoning sites. *Environ. Sci. Technol.* **2021**, *S5*, 9276–9284.
- (17) Xiong, S.; Chen, J.; Liu, H.; Chen, X.; Si, W.; Gong, Z.; Peng, Y.; Li, J. Like cures like: Detoxification effect between alkali metals and sulfur over the V₂O₅/TiO₂ deNO_x catalyst. *Environ. Sci. Technol.* **2022**, *S6*, 3739–3747.
- (18) Huang, L.; Zeng, Y.; Chang, Z.; Zong, Y.; Wang, H.; Zhang, S.; Yu, Y. Promotional effect of phosphorus modification on improving the Na resistance of V₂O₅-MoO₃/TiO₂ catalyst for selective catalytic reduction of NO_x by NH₃. *Mol. Catal.* **2021**, *S06*, No. 111565.
- (19) Huang, Z.; Gu, X.; Wen, W.; Hu, P.; Makkee, M.; Lin, H.; Kapteijn, F.; Tang, X. A "smart" Hollandite deNO_x catalyst: Self-protection against alkali poisoning. *Angew. Chem., Int. Ed.* **2013**, *S2*, 660–664.
- (20) Shen, Z.; Liu, X.; Impeng, S.; Zhang, C.; Yan, T.; Wang, P.; Zhang, D. Alkali and heavy metal copoisoning resistant catalytic reduction of NO_x via liberating Lewis acid sites. *Environ. Sci. Technol.* **2022**, *S6*, 5141–5149.
- (21) Zheng, L.; Zhou, M.; Huang, Z.; Chen, Y.; Gao, J.; Ma, Z.; Chen, J.; Tang, X. Self-protection mechanism of hexagonal WO₃-based deNO_x catalysts against alkali poisoning. *Environ. Sci. Technol.* **2016**, *S0*, 11951–11956.
- (22) Wang, P.; Wang, H.; Chen, X.; Liu, Y.; Weng, X.; Wu, Z. Novel SCR catalyst with superior alkaline resistance performance: Enhanced self-protection originated from modifying protonated titanate nanotubes. *J. Mater. Chem. A* **2015**, *3*, 680–690.
- (23) Mouljin, J. A.; van Diepen, A. E.; Kapteijn, F. Catalyst deactivation: is it predictable?: What to do? *Appl. Catal., A* **2001**, *212*, 3–16.
- (24) Kang, K.; Zhao, W.; Rong, J.; Luo, W.; Long, L.; Chen, Y.; Yao, X. Effect of H₂SO₄ pretreatment on alkali-resistance performance of FeZrCeTiO_x/TNT catalyst for NH₃-SCR reaction. *Appl. Surf. Sci.* **2022**, *S98*, No. 153774.
- (25) Song, J.; Impeng, S.; Zhang, J.; Deng, J.; Zhang, D. Elucidating the sensitivity of vanadyl species to water over V₂O₅/TiO₂ catalysts for NO_x abatement via operando Raman spectroscopy. *J. Catal.* **2022**, *416*, 198–208.
- (26) He, G.; Lian, Z.; Yu, Y.; Yang, Y.; Liu, K.; Shi, X.; Yan, Z.; Shan, W.; He, H. Polymeric vanadyl species determine the low-temperature activity of V-based catalysts for the SCR of NO_x with NH₃. *Sci. Adv.* **2018**, *4*, No. eaau4637.
- (27) Liu, X.; Wang, P.; Shen, Y.; Bi, S.; Ren, W.; Zhang, D. Boosting SO₂-tolerant catalytic reduction of NO_x via selective adsorption and activation of reactants over Ce₄₊-SO₄²⁻ pair sites. *ACS Catal.* **2022**, *12*, 11306–11317.
- (28) Kang, B.; Ceder, G. Battery materials for ultrafast charging and discharging. *Nature* **2009**, *458*, 190–193.
- (29) Mathew, V.; Kim, S.; Kang, J.; Gim, J.; Song, J.; Baboo, J. P.; Park, W.; Ahn, D.; Han, J.; Gu, L.; Wang, Y.; Hu, Y.-S.; Sun, Y.-K.; Kim, J. Amorphous iron phosphate: potential host for various charge carrier ions. *NPG Asia Mater.* **2014**, *6*, No. e138.
- (30) Liu, H.; Strobridge, F. C.; Borkiewicz, O. J.; Wiaderek, K. M.; Chapman, K. W.; Chupas, P. J.; Grey, C. P. Capturing metastable structures during high-rate cycling of LiFePO₄ nanoparticle electrodes. *Science* **2014**, *344* (issue), 6191.
- (31) Zhang, C.; Zhang, J.; Shen, Y.; He, J.; Qu, W.; Deng, J.; Han, L.; Chen, A.; Zhang, D. Synergistic Catalytic Elimination of NO_x and Chlorinated Organics: Cooperation of Acid Sites. *Environ. Sci. Technol.* **2022**, *S6*, 3719–3728.
- (32) Liu, S.; Kang, L.; Henzie, J.; Zhang, J.; Ha, J.; Amin, M. A.; Hossain, M. S. A.; Jun, S. C.; Yamauchi, Y. Recent Advances and Perspectives of Battery-Type Anode Materials for Potassium Ion Storage. *ACS Nano* **2021**, *S5*, 18931–18973.
- (33) Liu, J.; Cheng, H.; Zheng, H.; Zhang, L.; Liu, B.; Song, W.; Liu, J.; Zhu, W.; Li, H.; Zhao, Z. Insight into the potassium poisoning effect for selective catalytic reduction of NO_x with NH₃ over Fe/Beta. *ACS Catal.* **2021**, *11*, 14727–14739.
- (34) Zhu, Y.-m.; Ruan, Z.-w.; Tang, S.-z.; Thangadurai, V. Research status in preparation of FePO₄: a review. *Ionics* **2014**, *20*, 1501–1510.
- (35) Burba, C. M.; Palmer, J. M.; Holinsworth, B. S. Laser-induced phase changes in olivine FePO₄: a warning on characterizing LiFePO₄-based cathodes with Raman spectroscopy. *J. Raman Spectrosc.* **2009**, *40*, 225–228.
- (36) Zhao, R.; Pang, R.; Wang, Y.; Zhao, Z. Effect of metal elements doping on the CePO₄ catalysts for selective catalytic reduction of NO with NH₃. *Mol. Catal.* **2022**, *S30*, No. 112627.
- (37) Voronin, V. I.; Ponosov, Y. S.; Berger, I. F.; Proskurnina, N. V.; Zubkov, V. G.; Tyutyunnik, A. P.; Bushmeleva, S. N.; Balagurov, A. M.; Sheptyakov, D. V.; Burmakin, E. I.; Shekhtman, G. S.; Vovkotrub, E. G. Crystal structure of the low-temperature form of K₃PO₄. *Inorg. Mater.* **2006**, *42*, 908–913.
- (38) Zaghib, K.; Julien, C. M. Structure and electrochemistry of FePO₄·2H₂O hydrate. *J. Power Sources* **2005**, *142*, 279–284.
- (39) Zhang, L.; Brow, R. K. A Raman study of iron–phosphate crystalline compounds and glasses. *J. Am. Ceram. Soc.* **2011**, *94*, 3123–3130.
- (40) Xu, J.; Chen, G.; Guo, F.; Xie, J. Development of wide-temperature vanadium-based catalysts for selective catalytic reducing of NO_x with ammonia: Review. *Chem. Eng. J.* **2018**, *353*, 507–518.
- (41) Grosvenor, A. P.; Kobe, B. A.; Biesinger, M. C.; McIntyre, N. S. Investigation of multiplet splitting of Fe 2p XPS spectra and bonding in iron compounds. *Surf. Interface Anal.* **2004**, *36*, 1564–1574.
- (42) Jiang, F.; Wang, S.; Liu, B.; Liu, J.; Wang, L.; Xiao, Y.; Xu, Y.; Liu, X. Insights into the influence of CeO₂ crystal facet on CO₂ hydrogenation to methanol over Pd/CeO₂ catalysts. *ACS Catal.* **2020**, *10*, 11493–11509.
- (43) Dong, Y.; Wang, P.; Liu, X.; Deng, J.; Chen, A.; Han, L.; Zhang, D. Alkali-resistant NO_x reduction over FeVO₄/TiO₂ catalysts via regulating the electron transfer between Fe and V. *Chin. Chem. Lett.* **2023**, No. 108635.
- (44) Zhao, Y.; Shi, L.; Shen, Y.; Zhou, J.; Jia, Z.; Yan, T.; Wang, P.; Zhang, D. Self-Defense Effects of Ti-Modified Attapulgite for Alkali-Resistant NO_x Catalytic Reduction. *Environ. Sci. Technol.* **2022**, *S6*, 4386–4395.
- (45) Zhou, J.; Wang, P.; Chen, A.; Qu, W.; Zhao, Y.; Zhang, D. NO_x Reduction over Smart Catalysts with Self-Created Targeted Antipoisoning Sites. *Environ. Sci. Technol.* **2022**, *S6*, 6668–6677.
- (46) Li, S.; Yu, H.; Lan, T.; Shi, L.; Cheng, D.; Han, L.; Zhang, D. NO_x reduction against alkali poisoning over Ce(SO₄)₂-V₂O₅/TiO₂ catalysts by constructing the Ce₄₊-SO₄²⁻ pair sites. *Chin. Chem. Lett.* **2023**, No. 108240.
- (47) Hu, X.; Huang, L.; Zhang, J.; Li, H.; Zha, K.; Shi, L.; Zhang, D. Facile and template-free fabrication of mesoporous 3D nanosphere-like Mn_xCo_{3-x}O₄ as highly effective catalysts for low temperature SCR of NO_x with NH₃. *J. Mater. Chem. A* **2018**, *6*, 2952–2963.
- (48) Kumar, P. A.; Jeong, Y. E.; Gautam, S.; Ha, H. P.; Lee, K. J.; Chae, K. H. XANES and DRIFTS study of sulfated Sb/V/Ce/TiO₂ catalysts for NH₃-SCR. *Chem. Eng. J.* **2015**, *275*, 142–151.
- (49) Chen, L.; Si, Z.; Wu, X.; Weng, D. DRIFT study of CuO-CeO₂-TiO₂ mixed oxides for NO_x reduction with NH₃ at low temperatures. *ACS Appl. Mater. Interfaces* **2014**, *6*, 8134–8145.
- (50) Liu, J.; Li, X.; Zhao, Q.; Ke, J.; Xiao, H.; Lv, X.; Liu, S.; Tadé, M.; Wang, S. Mechanistic investigation of the enhanced NH₃-SCR on cobalt-decorated Ce-Ti mixed oxide: *In situ* FTIR analysis for

structure-activity correlation. *Appl. Catal. B: Environ.* **2017**, *200*, 297–308.

(51) Liu, S.-w.; Guo, R.-t.; Sun, X.; Liu, J.; Pan, W.-g.; Shi, X.; Wang, Z.-y.; Liu, X.-y.; Qin, H. Selective catalytic reduction of NO_x over Ce/TiZrO_x catalyst: The promoted K resistance by TiZrO_x support. *Mol. Catal.* **2019**, *462*, 19–27.

(52) Janssens, T. V. W.; Falsig, H.; Lundsgaard, L. F.; Vennestrøm, P. N. R.; Rasmussen, S. B.; Moses, P. G.; Giordanino, F.; Borfecchia, E.; Lomachenko, K. A.; Lamberti, C.; Bordiga, S.; Godiksen, A.; Mossin, S.; Beato, P. A consistent reaction scheme for the selective catalytic reduction of nitrogen oxides with ammonia. *ACS Catal.* **2015**, *5*, 2832–2845.

(53) Hadjiivanov, K. I. Identification of neutral and charged N_xO_y surface species by IR spectroscopy. *Catal. Rev.* **2000**, *42*, 71–144.

(54) Lyu, M.; Zou, J.; Liu, X.; Yan, T.; Wang, P.; Zhang, D. Insight on the anti-poisoning mechanism of *in situ* coupled sulfate over iron oxide catalysts in NO_x reduction. *Catal. Sci. Technol.* **2022**, *12*, 4020–4031.

(55) Weng, X.; Dai, X.; Zeng, Q.; Liu, Y.; Wu, Z. DRIFT studies on promotion mechanism of $\text{H}_3\text{PW}_{12}\text{O}_{40}$ in selective catalytic reduction of NO with NH₃. *J. Colloid Interface Sci.* **2016**, *461*, 9–14.

(56) Marberger, A.; Ferri, D.; Elsener, M.; Krocher, O. The Significance of Lewis Acid Sites for the Selective Catalytic Reduction of Nitric Oxide on Vanadium-Based Catalysts. *Angew. Chem. Int. Ed.* **2016**, *55*, 11989–11994.

□ Recommended by ACS

Facile H₂O-Contributed O₂ Activation Strategy over Mn-Based SCR Catalysts to Counteract SO₂ Poisoning

Dongqi An, Lin Dong, *et al.*

SEPTEMBER 22, 2023

ENVIRONMENTAL SCIENCE & TECHNOLOGY

READ ↗

Theoretical Investigation of the Alkali Metal Poisoning Tolerance Mechanism of CeO₂-Containing Fe and H₂SO₄ Additives

Kai Oshiro, Jun-ya Hasegawa, *et al.*

SEPTEMBER 18, 2023

THE JOURNAL OF PHYSICAL CHEMISTRY C

READ ↗

Anti-Poisoning Mechanisms of Sb on Vanadia-Based Catalysts for NO_x and Chlorobenzene Multi-Pollutant Control

Xing Yuan, Junhua Li, *et al.*

JULY 10, 2023

ENVIRONMENTAL SCIENCE & TECHNOLOGY

READ ↗

Mechanistic Insight into Catalytic Combustion of Ethyl Acetate on Modified CeO₂ Nanobelts: Hydrolysis–Oxidation Process and Shielding Effect of Acetates/Alcoholates

Zude Shen, Qiguang Dai, *et al.*

FEBRUARY 22, 2023

ENVIRONMENTAL SCIENCE & TECHNOLOGY

READ ↗

Get More Suggestions >